Chinese Journal of
POLYMER SCIENCE

RESEARCH ARTICLE

https://doi.org/10.1007/s10118-026-3623-8
Chinese J. Polym. Sci. **2026**, *44*, 2212–2225

Hypercrosslinked Porous Organic Polymers from Tetraaniline and Anthraquinone for High-capacitance, Long-life Supercapacitors

Xiao-Qian Gong†, Xin-Ze-Yu Zhang†, Yi-Fei Zhou, Yi Shi, Yu-Meng Zhang, Jia-Wei Hu, Peng-Cheng Li, Wei Lyu*, and Yao-Zu Liao*

State Key Laboratory of Advanced Fiber Materials, College of Materials Science and Engineering, Donghua University, Shanghai 201620, China

Electronic Supplementary Information

Abstract Hypercrosslinked polymers (HCPs) are promising electrode materials for supercapacitors owing to their rigid three-dimensional networks and excellent structural stability; however, their electrochemical performance is often limited by an over-reliance on electric double-layer capacitance or insufficient redox-active sites. Herein, we report a series of hypercrosslinked polymers (HCPs) constructed from tetraaniline (TANI) and 2,6-diaminoanthraquinone (DAQ) to integrate abundant redox-active sites with robust three-dimensional porous networks for high-capacitance and long-life supercapacitor electrodes. By tuning the TANI-to-DAQ molar ratio, the optimized TADA11-HCP exhibits a hierarchical micro-/mesoporous architecture for exposed active sites and facilitated mass diffusion, along with the lowest optical bandgap (acid-treated) among the series for fast electron transport. Benefiting from the combined advantages of structural strength, hierarchical porosity, and an optimized electronic structure, TADA11-HCP achieves 700 $F{\cdot}g^{-1}$ at 1 $A{\cdot}g^{-1}$ and retains 92% capacitance after 10000 cycles, demonstrating excellent cycling stability. A flexible quasi-solid-state symmetric supercapacitor further demonstrates 278.4 $F{\cdot}g^{-1}$ and an energy density of 38.7 $Wh{\cdot}kg^{-1}$, highlighting the practical potential of TADA-HCPs for advanced supercapacitor applications. This work demonstrates an effective molecular-level strategy to enhance the capacitance of HCP-based electrodes while maintaining long-term stability, providing insights into the rational design of high-performance HCPs for supercapacitor applications.

Keywords Tetraaniline; Hypercrosslinked polymer; Supercapacitor; High-capacitance; Long-life

Citation: Gong, X. Q.; Zhang, X. Z. Y.; Zhou, Y. F.; Shi, Y.; Zhang, Y. M.; Hu, J. W.; Li, P. C.; Lyu, W.; Liao, Y. Z. Hypercrosslinked porous organic polymers from tetraaniline and anthraquinone for high-capacitance, long-life supercapacitors. *Chinese J. Polym. Sci.* **2026**, *44*, 2212–2225.

INTRODUCTION

Nowadays, the inherent intermittency of renewable sources, together with the rapid expansion of electric vehicles, portable electronics, and smart grid systems, has driven the growing demand for high-efficiency energy-storage technologies.[1–3] Within this context, supercapacitors have become one of indispensable electrochemical storage devices. By simultaneously delivering high power output, rapid charge-discharge on the millisecond scale, prolonged cycling lifetime, and wide temperature adaptability, these systems overcome the intrinsic performance limitations of separating conventional capacitors from secondary batteries.[4,5]

Supercapacitors can be classified into two main types: electric double-layer capacitors and pseudocapacitors, according to their underlying charge-storage mechanisms.[6] Among the pseudocapacitive electrode materials, polyaniline (PANI) has received considerable attention due to its unique electrochemical activity, facile synthesis, and environmental compatibility.[7,8] Tetraaniline (TANI), the shortest aniline oligomer of PANI, retains the reversible redox activity and distinctive doping-responsive behavior inherent to PANI. TANI has demonstrated a superior specific capacitance owing to its well-defined molecular and crystal structures.[9,10] However, frequent electrochemical doping and dedoping processes cause pronounced volumetric changes in TANI, accelerating the short chain's degradation.[11] Several strategies, like compositing with conductive carbon materials, crystallization engineering and *in situ* grafting, have been devoted to improve TANI's stability for supercapacitor electrode.[11–14] For instance, Lee *et al*. physically loaded TANI onto the surface of graphene oxide (GO) sheets *via* chemical oxidative polymerization, forming a core-shell structured composite. Owing to the combined contributions of the pseudocapacitive TANI and conductive GO, the specific capacitance of this composite electrode reached 769 $F{\cdot}g^{-1}$ at 1 $A{\cdot}g^{-1}$. The two-dimensional layered framework of GO not only effectively suppresses the dissolution of TANI in the electrolyte, but also provides robust mechanical support and buffering capacity to accom-

* Corresponding authors, E-mail: wlyu@dhu.edu.cn (W.L.)
E-mail: yzliao@dhu.edu.cn (Y.Z.L.)
† These authors contributed equally to this work.
Received December 23, 2025; Accepted February 14, 2026; Published online June 22, 2026

modate the volumetric changes of the polymer during charge-discharge cycling. As a result, after 2000 charge-discharge cycles, the composite maintains 90.2%–95.1% capacitance retention, significantly enhancing the structural stability of TANI during prolonged cycling.[12] Shao *et al*. enhanced the conductivity and structural rigidity of TANI through the synthesis of crystalline TANI nanosheets. In a neutral NaCl electrolyte, charge storage proceeds *via* the reversible insertion/extraction of chloride ions, effectively circumventing the degradation issues associated with the conventional proton-doping mechanism. Consequently, the crystalline TANI electrode achieves 600.7 F·g^{-1} specific capacitance at 2 mV·s^{-1} and maintains 84.4% capacitance retention after 2000 cycles.[13] Kaner *et al*. employed perfluorophenylazide (PFPA)-mediated coupling chemistry to covalently graft TANI molecules onto a three-dimensional graphene scaffold to construct an ATgGN composite. This robust covalent interface firmly anchors the active material to the conductive network, effectively suppressing material detachment and agglomeration during charge-discharge cycles. At 1 A·g^{-1}, the ATgGN electrode achieved an impressive specific capacitance of 278 F·g^{-1}, accompanied by 85% capacitance retention over 30000 charge-discharge cycles.[14] Although these efforts, achieving both high capacitance and stability is still desirable.

Recently, hypercrosslinked polymers (HCPs), where are three-dimensional network materials formed by densel covalent crosslinking of molecular building blocks through rigid short spacers, have attracted increasing interest for the fabrication of robust functional porous networks.[15] The main interest stems from the fact that they can retain permanent intrinsic microporosity after solvent removal, yielding a high surface area, abundant nanoscale channels, and excellent physicochemical stability.[16–18] The merits of this strategy have been preliminarily validated in energy-storage applications.[19–23] As electrode materials for supercapacitors, HCPs have mainly been explored through three representative strategies. In many cases, HCPs have been employed as porous frameworks or precursors to provide large surface areas for electric double-layer charge storage, which generally ensures excellent cycling durability but often results in limited capacitance enhancement due to the lack of intrinsic redox-active sites.[20] To introduce pseudocapacitive behavior, redox-functional units such as quinone or carbonyl moieties have also been incorporated into HCP backbones. For instance, Mohamed *et al*. synthesized a tetraphenylanthraquinone-based HCP (An-CPOP-2) with a Brunauer-Emmett-Teller (BET) specific surface area (S_{BET}=1130 m^2·g^{-1}) that exhibited a capacitance of 98.4 F·g^{-1} and 95.3% capacitance retention after 2000 cycles.[21] Similarly, Goudar *et al*. reported a HCP with electron-deficient π-system (BPI-HCP-I). This material possessed a high S_{BET} of 544 m^2·g^{-1} with a hierarchical pore size distribution (0.9–2.6 nm). When employed as a supercapacitor electrode, BPI-HCP-I achieved 112 F·g^{-1} capacitance at 5 mV·s^{-1}. Furthermore, it maintained 90% capacity after 4000 charge-discharge cycles in an acidic electrolyte.[22] While these studies demonstrate the excellent structural stability and durability of HCP-based electrodes, their capacitive performance is often constrained by the limited density or utilization efficiency of electroactive sites. Alternatively, composite strategies combining HCPs with conducting polymers have been developed to improve capacitance by introducing additional redox activity. For instance, a PANI/HCP composite (PANI@SOAM-Cy HCP) was further developed, delivering 678 F·g^{-1} and preserving 81.9% of its initial capacitance over 5000 cycles.[23] However, such composite architectures may suffer from interfacial mismatch, nonuniform distribution of active components, and complicated charge/ion transport pathways, which can compromise long-term reliability and limit further performance optimization. Overall, these studies indicate that although hypercrosslinking provides an effective route toward constructing porous electrodes with high stability, it remains challenging to simultaneously realize abundant redox activity, efficient charge utilization, and structural robustness within a single, molecularly integrated HCP framework.

In this study, we report HCPs from TANI and anthraquinone (AQ) with numerous active sites for pseudocapacitive energy storage, high porosity for electric double-layer energy storage, and improved structural robustness for an extended cycle life. TANI served as the key conductive building block, which was hypercrosslinked with 2,6-diaminoanthraquinone (DAQ)—a quinone-rich unit—through methylene bridges (TADA-HCPs). TADA-HCPs not only integrate the redox activity of TANI and AQ, but also exhibit high porosity arising from the hypercrosslinked three-dimensional network. By systematically adjusting the initial molar ratio of TANI to DAQ, TADA11-HCP obtained at a 1:1 ratio, showed a hierarchical pore structure, characterized by micropores centered at approximately 1.6 nm and mesopores spanning 2–20 nm for exposed active sites and facilitated mass diffusion, it also exhibited the lowest optical bandgap of 1.26 eV (acid-treated) among the series, suggesting enhanced π-electron delocalization and improved electronic conductivity.

Therefore, it showed an impressive specific capacitance (700 F·g^{-1} at 1 A·g^{-1}), coupled with outstanding sustained cycling performance, maintaining 91% after 1×10^4 cycles at 2 A·g^{-1} within a three-electrode configuration. In contrast, the pristine TANI electrode demonstrated a capacitance of 618 F·g^{-1} under the same conditions, but suffered from severe capacity fading, retaining only 33% of its original capacitance. To verify its practical applicability, we successfully designed a flexible quasi-solid-state symmetric supercapacitor incorporating a poly(vinyl alcohol) (PVA)/H_2SO_4 gel electrolyte, with TADA11-HCP as the electrode material. At 1 A·g^{-1}, the device exhibited a capacitance of 278.4 F·g^{-1}. Meanwhile, the device delivered 38.7 Wh·kg^{-1} at 500.43 W·kg^{-1}, demonstrating competitive energy-storage capabilities. Moreover, by connecting multiple devices in series, a row of commercial yellow LEDs were powered, highlighting the practical capabilities of the device. The synthesized TADA-HCPs presented a promising solution for the construction of next-generation supercapacitor electrodes with long cycle stability and high power density.

EXPERIMENTAL

Materials

2,6-Diaminoanthraquinone (DAQ, >97.0%) was acquired from

TCI (Shanghai) Chemical Industry Development Co., Ltd. Diiodomethane (CH_2I_2, RG, 99%+, stabilized with copper) and *N*,*N*-dimethylformamide (DMF, anhydrous, water ≤50 ppm water) were obtained from Shanghai Titan Co., Ltd. Anhydrous potassium carbonate (K_2CO_3, ≥98.0%) was acquired from Sinopharm Chemical Reagent Co., Ltd. TANI was synthesized according to the procedure outlined by Zhang *et al*. *via* oxidative coupling of *N*-phenyl-1,4-phenylenediamine under acidic conditions.

Preparation of Hypercrosslinked Polymers (TADA-HCPs)

The TADA-HCPs were synthesized *via* a microwave-assisted *N*-alkylation reaction, following a typical hypercrosslinking polymerization protocol (Fig. 1a).[17] Initially, under a continuous inert nitrogen atmosphere, tetraaniline (0.2 mmol, 0.06 g), 2,6-diaminoanthraquinone (0.1 mmol, 19.5 mg), anhydrous K_2CO_3 (7.24 mmol, 1 g), and anhydrous DMF (10 mL) were sequentially charged into a dry 20 mL microwave vial. Following complete dissolution of the solids, diiodomethane (2 mL) was introduced as the crosslinker. Upon sealing, the vial was placed into a microwave reactor. The reaction mixture was heated at 100 °C for 20 min, after which it was ramped to 130 °C and held for 1 h. After cooling to ambient temperature, the crude material was isolated *via* vacuum filtration, followed by a thorough cleaning with DMF, deionized water, and ethanol remove inorganic salts, catalyst residues, and unreacted monomers. Further purification involved Soxhlet extraction with DMF over 24 h. Finally, the material was vacuum-dried at 80 °C for 24 h. To yield a dark hypercrosslinked polymer powder, designated as TADA21-HCP. Control experiments were carried out using the same procedure but with different amounts of DAQ, 0.2 mmol (0.039 g) and 0.4 mmol (0.078 g), affording the polymers denoted as TADA11-HCP and TADA12-HCP, respectively.

Materials Characterization

The comprehensive properties of the TADA-HCPs, including their chemical composition, physical form, thermal resilience, and pore arrangement, were thoroughly analyzed using multiple methodologies. A Nicolet 6700 spectrometer was utilized to acquire Fourier transform infrared (FTIR) spectra, which provided a detailed analysis of the functional groups and chemical bonds present in the materials under investigation. The samples' microstructure and surface topography were meticulously examined with a Zeiss Gemini SEM 500, a high-end field-emission scanning electron microscope (SEM). With the advanced Thermo Scientific ESCALAB 250Xi equipment, X-ray photoelectron spectroscopy (XPS) analyzed the sample's elemental composition and chemical state. The thermal properties were assessed using a NETZSCH Libra 2F1 thermogravimetric analyzer (TGA), with samples heated at 10 °C·min^{-1} from 30 °C to 900 °C in a nitrogen atmosphere. UV-Vis diffuse reflectance spectra (200–1400 nm) were measured using a UV-2610 spectrophotometer, which includes an integrating sphere for enhanced reflectance analysis. A Bruker D8 ADVANCE diffractometer was employed for X-ray diffraction (XRD) analysis of the crystalline structure, utilizing Cu Kα radiation (λ=1.5406 Å). The scanning range was set as 2θ=5°–90° at 1200 W. At about −196 °C, the Micromeritics ASAP 2020 physical adsorption analyzer was employed to acquire N_2 adsorption-desorption isotherms, revealing data on the specific surface area and pore structure of the material. A Bruker AVANCE 400 NMR spectrometer was employed to obtain solid-state (^{13}C CP/MAS NMR) spectra to analyze polymer molecular architecture

Electrochemical Testing

A Gamry Interface 1100E electrochemical workstation was employed to perform cyclic voltammetry (CV), electrochemical impedance spectroscopy (EIS), and galvanostatic charge-discharge (GCD) measurements. In the preparation of the working electrode, TADA-HCPs, conductive carbon black, and PVDF were blended in a 7:2:1 weight proportion, followed by the addition of NMP as a solvent. The resulting mixture was subsequently pulverized into a uniform blend. The slurry was evenly distributed across the pretreated carbon paper current collectors before being placed in vacuum oven at 60 °C overnight, which guaranteed that no residual solvent remained. The loading of TADA-HCPs was maintained at roughly 1.0 mg·cm^{-2} on the electrodes. Electrochemical performance evaluation was conducted employing a three-electrode configuration, with the electrolytic medium being a 1.0 mol·L^{-1} H_2SO_4 solution. The working electrode was pretreated, the counter electrode consisted of a graphite rod, with Ag/AgCl (saturated KCl) serving as the reference. To assess the practical performance of the optimized material in the device configuration, a symmetric supercapacitor was assembled. In this two-electrode system, two identical electrodes fabricated using the optimal TADA material were used as both positive and negative electrodes, and the electrolyte was 1.0 mol·L^{-1} H_2SO_4 aqueous solution. To further investigate the material's performance in practical applications, the device was subsequently assembled into a quasi-solid-state symmetric supercapacitor, utilizing PVA/H_2SO_4 gel as the electrolyte.

RESULTS AND DISCUSSION

Structural and Morphological Characterization of TADA-HCPs

FTIR, solid-state ^{13}C-NMR and XPS spectra were performed to confirm the successful hypercrosslinking reaction between the TANI and DAQ *via* methylene (—CH_2—) bridges. Fig. 1(b) shows the FTIR spectra of TANI, DAQ, and TADA-HCPs. The observed two new distinct bands at 2927 and 2860 cm^{-1} in the TADA-HCPs are attributed to the asymmetric and symmetric stretching vibrations in —CH_2— groups, respectively, indicating successful crosslinking reaction of TANI and DAQ with diiodomethane.[24] The observed sharp absorption band at 1665 cm^{-1} of TADA-HCPs is originates from the C=O stretching vibration of the AQ units in DAQ.[25] The 1580 and 1500 cm^{-1} bands correspond to the C=C skeletal vibrations in quinoid and benzenoid rings of TANI, respectively.[26] It can be seen that with the increasing DAQ content, the quinoid peak intensity becomes progressively stronger, as well as the intensity of —NH— characteristic bond located at 3350 cm^{-1}, indicating successful incorporation of AQ units. In the solid-state ^{13}C-NMR profiles of the TADA-HCPs (Fig. 1c), a characteristic peak at δ=181 ppm was assigned to the carbonyl carbon (C=O) in the AQ moieties, confirming that DAQ units are integrated into the polymer backbone.[27] With increasing DAQ content from TADA21-HCP to TADA12-HCP, this C=O resonance showed an enhanced intensity together with a slight downfield shift, which is consistent with the higher concentration of carbonyl groups and a modi-

fied local electronic environment of the carbonyl carbons. Such a shift may be associated with stronger electronic interactions within the polymer framework induced by the increased DAQ fraction.[28] The broad and intense signal observed in the range of δ=30–50 ppm corresponds to the carbon atoms of $-CH_2-$.[29,30] In addition, a set of overlapping signals over δ=100–165 ppm arises from all aromatic carbons in the TANI and AQ units, including benzenoid and quinoid rings.[26,27,31] XPS analysis further corroborates the chemical structure from a surface-sensitive perspective. In the C 1s spectra, the peak intensity at 287.0 eV, corresponding to the C=O group, increases with the nominal DAQ content (Fig. 1d).[25] The relative peak area of C=O rises from 11% for TADA21-HCP to 13% for TADA11-HCP and further to 16% for TADA12-HCP. In the N 1s spectra, a relative area of a distinct peak observed at 400.8 eV, corresponding to nitrogen atoms covalently bonded to three carbon atoms ($N-C_3$), is 18%, 19%, and 17% for TADA21-HCP, TADA11-HCP, and TADA12-HCP, respectively (Fig. 1e).[14] The highest $N-C_3$ contribution in TADA11 indicates a higher crosslinking density in this sample. XRD patterns of TADA-HCPs display broad diffraction peaks around $2\theta \approx 18°–25°$, rather than sharp crystalline peaks, which are characteristic of amorphous materials and consistent with the expected structure of irreversibly formed hypercrosslinked polymers (Fig. S2 in the electronic supplementary information, ESI). Subtle variations in the diffraction features suggest changes in molecular packing induced by increasing DAQ content in the TADA-HCPs.[32]

Fig. 1(f) shows the nitrogen adsorption-desorption isotherm, in which TADA21-HCP and TADA11-HCP exhibit typical Type II characteristics, indicating multilayer adsorption and reflecting a moderate level of porosity. In contrast, TADA12-HCP displays a distinct Type IV profile accompanied by a pronounced H3-type hysteresis loop. This behavior confirms the presence of a well-developed mesoporous structure, where the pores are likely derived from slit-shaped interparticle voids generated by nanoparticle stacking.[33] The calculated S_{BET}s of TADA21-HCP, TADA11-HCP, and TADA12-HCP are 110, 114, and 131 $m^2 \cdot g^{-1}$, respectively. Further non-local density functional theory (NLDFT) analysis of pore-size distribution (Fig. 1g) indicates that TADA21-HCP and TADA11-HCP have micropores around 1.6 nm and mesopores between 2 and 20 nm. This indicates a hierarchical micro-/mesoporous architecture. In contrast, TADA12-HCP exhibits a mesopore-dominated structure with a main pore-size maximum around 3.7 nm, while retaining a distinct micropore contribution near 1.7 nm. As the SEM images shown in Fig. S3 (in ESI), TADA-HCPs shows the morphology of aggregated nanoparticles. The stacking of these nanoparticles may lead to large mesopores formation.[22] To further clarify the influence of crosslinking degree on the pore structure, the total pore volume and micropore fraction were compared (Table S1 in ESI). Although TADA12-HCP exhibits the highest S_{BET}, it shows the lowest micropore volume ratio (0.011 $cm^3 \cdot g^{-1}$, 4.7%), indicating that its surface area mainly originates from mesopores formed by interparticle stacking (H3-type hysteresis). In contrast, TADA11-HCP with the highest crosslinking degree possesses the largest micropore fraction (0.021 $cm^3 \cdot g^{-1}$, 7.2%), suggesting a more rigid and densely crosslinked network with intrinsically generated micropores, which is beneficial for exposing redox-active sites and facilitating efficient charge storage. As shown in the TGA curves in Fig. S4 (in ESI), the TANI and TADA-HCPs exhibited distinct thermal decomposition behaviors reflecting their different molecular architectures. For TANI, a gradual weight loss occurred in the range of approximately 180–300 °C, which can be attributed to the decomposition of residual dopants, terminal oligomeric segments, and relatively unstable conjugated units. The subsequent major weight loss starting near about 300 °C is mainly associated with the thermal degradation of the aromatic aniline backbone, accompanied by partial carbonization.[34] In contrast, all TADA-HCPs display a clearly delayed decomposition profile. A minor weight loss below about 100 °C arises from physically adsorbed moisture, while the gradual mass loss at around 200–336 °C is attributed to the release of residual solvent molecules trapped within the rigid porous network. The primary decomposition stage beginning at around 336 °C corresponds to the cleavage of methylene ($-CH_2-$) crosslinking bridges together with the degradation of the aromatic framework, followed by carbonization.[24,35] The results showed that the hypercrosslinked structure greatly improved the thermal stability of the materials. Among the series, TADA11-HCP showed particularly good thermal stability, retaining a high char yield of approximately 45% at 800 °C, which further indicated the superior structural integrity of its highly crosslinked network.

Electrochemical Testing

The electrochemical properties of the TANI and TADA-HCPs were systematically evaluated within a three-electrode setup employing 1.0 $mol \cdot L^{-1}$ H_2SO_4 as the electrolyte. CV measurements were first conducted at a scanning rate of 5–50 $mV \cdot s^{-1}$ (Fig. 2e, and Fig. S5 in ESI). Fig. 2(a) displays the representative CV profiles of all materials at 20 $mV \cdot s^{-1}$ within a 0–0.9 V window (versus Ag/AgCl). As observed, all the TADA-HCP electrodes exhibited two distinct oxidation peaks (denoted as O1 and O2) and two reduction peaks (R1 and R2) within the tested potential window, indicating the involvement of multiple reversible Faradaic redox processes. These redox features were primarily due to the redox-active $-N=$ moieties of TANI and the C=O functional groups of the AQ units, highlighting the pronounced pseudocapacitive characteristics of the TADA-HCP electrodes.[26,36] Notably, the CV curves deviate significantly from the ideal rectangular shape seen in electric double-layer capacitors, suggesting that charge storage is mainly controlled by reversible Faradaic reactions rather than pure electrostatic adsorption. Moreover, a comparison of the integrated CV areas revealed that TADA11-HCP encloses a substantially larger area than pristine TANI and the other TADA-HCP samples, indicating its superior charge-storage capability and the highest initial specific capacitance.[37] The capacitive properties were further quantified by GCD measurements within the same voltage window at 1 $A \cdot g^{-1}$ to 10 $A \cdot g^{-1}$ (Fig. S6 in ESI). The GCD profile of TADA11-HCP displays excellent symmetry and a pronounced discharge plateau, confirming its dominant pseudocapacitive character and high electrochemical reversibility.[38] Fig. 2(b) summarizes the specific capacitance of all materials versus current density. TADA11-HCP delivers the maximum capacitance of 700 $F \cdot g^{-1}$ at a rate of 1 $A \cdot g^{-1}$, corresponding to its greatest cyclic voltammetry area under the curve. Even at 10 $A \cdot g^{-1}$, it retains a

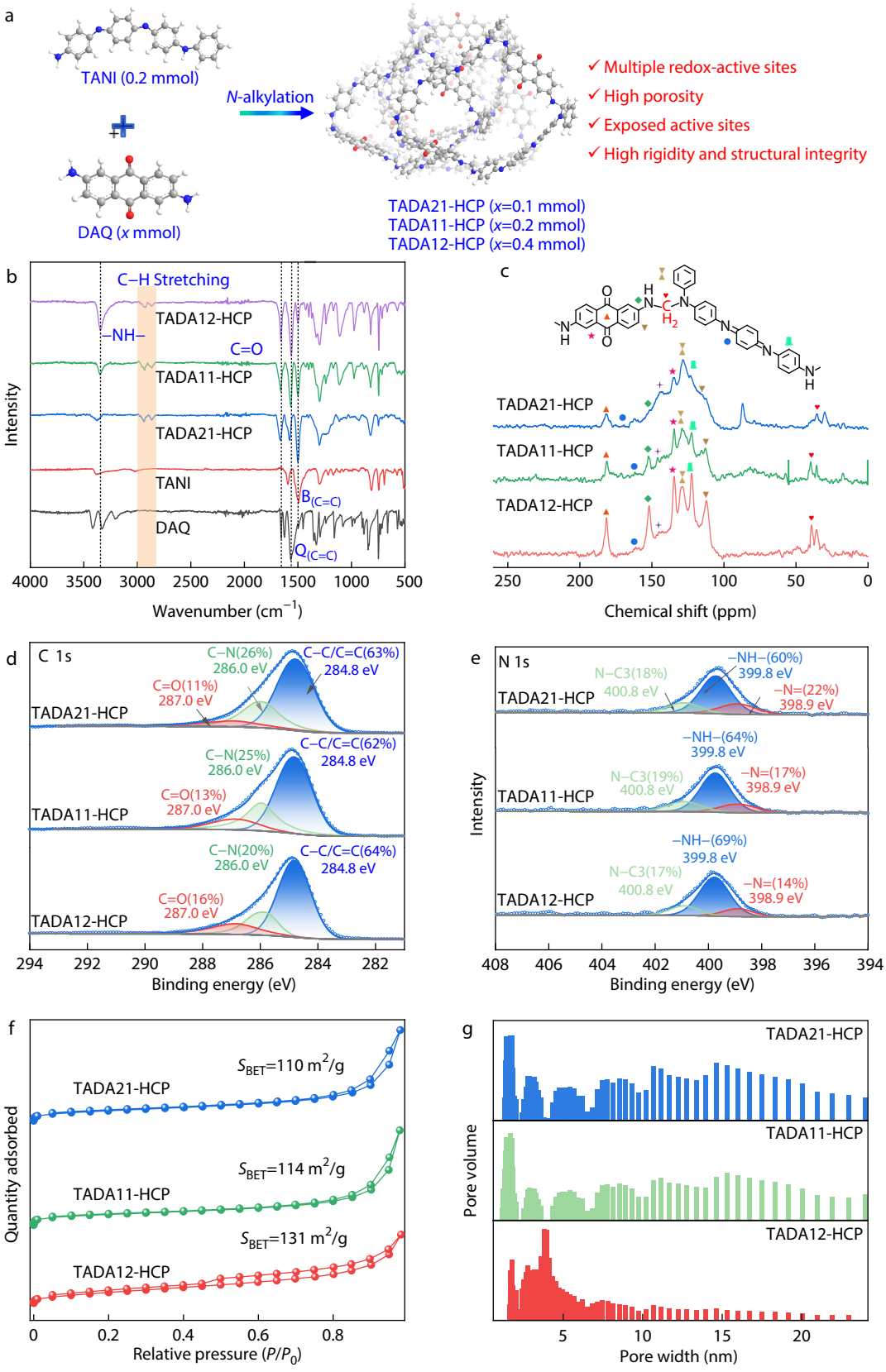

Fig. 1 (a) Synthesis routes to TADA-HCPs; (b) FTIR spectra of TANI and TADA-HCPs; (c) ^{13}C TADA-HCPs NMR spectra; (d) C 1s XPS spectra of TADA-HCPs; (e) N 1s XPS spectra of TADA-HCPs; (f) N_2 adsorption-desorption isotherms of TADA-HCPs; (g) Pore size distributions for TADA-HCP.

https://doi.org/10.1007/s10118-026-3623-8

capacitance of about 454 F·g^{-1}, corresponding to a capacity retention of about 65% and outperforming all other samples, demonstrating its better rate capability. EIS was conducted to investigate the kinetics and interfacial behavior, Fig. 2(c) presents the Nyquist plots along with their corresponding equivalent-circuit fits. All electrodes show a small high-frequency intercept with the real axis, reflecting low solution resistance and good electrical contact.[37,39] The fitted charge-transfer resistance (R_{ct}) values are 0.74 Ω (TADA21-HCP), 0.57 Ω (TADA11-HCP), and 1.3 Ω (TADA12-HCP). The lowest R_{ct} of TADA11-HCP signifies the most rapid faradaic kinetics at the electrode/electrolyte interface, consistent with its excellent pseudocapacitive performance in CV and GCD tests. Furthermore, the steepest low-frequency slope in the Nyquist plot for TADA11-HCP reflects more ideal capacitive characteristics and efficient ion-diffusion dynamics, which is largely due to its hierarchical micro-/mesoporous architecture, where micropores provide abundant electroactive sites and interconnected mesopores facilitate rapid ion transport.[40] The kinetic behavior can be further rationalized by the intrinsic electronic structure of the materials, as reflected in their optical band gaps (E_g). Tauc-plot analysis of UV-Vis spectra under acidic conditions yields E_g values of 1.06 eV (TANI), 1.32 eV (TADA21-HCP), 1.26 eV (TADA11-HCP), and 1.47 eV (TADA12-HCP) (Figs. S7 and S8 in ESI). The relatively narrow band gap of TADA11-HCP (1.26 eV) indicates enhanced intrinsic conductivity, which aligns with its record-low charge-transfer

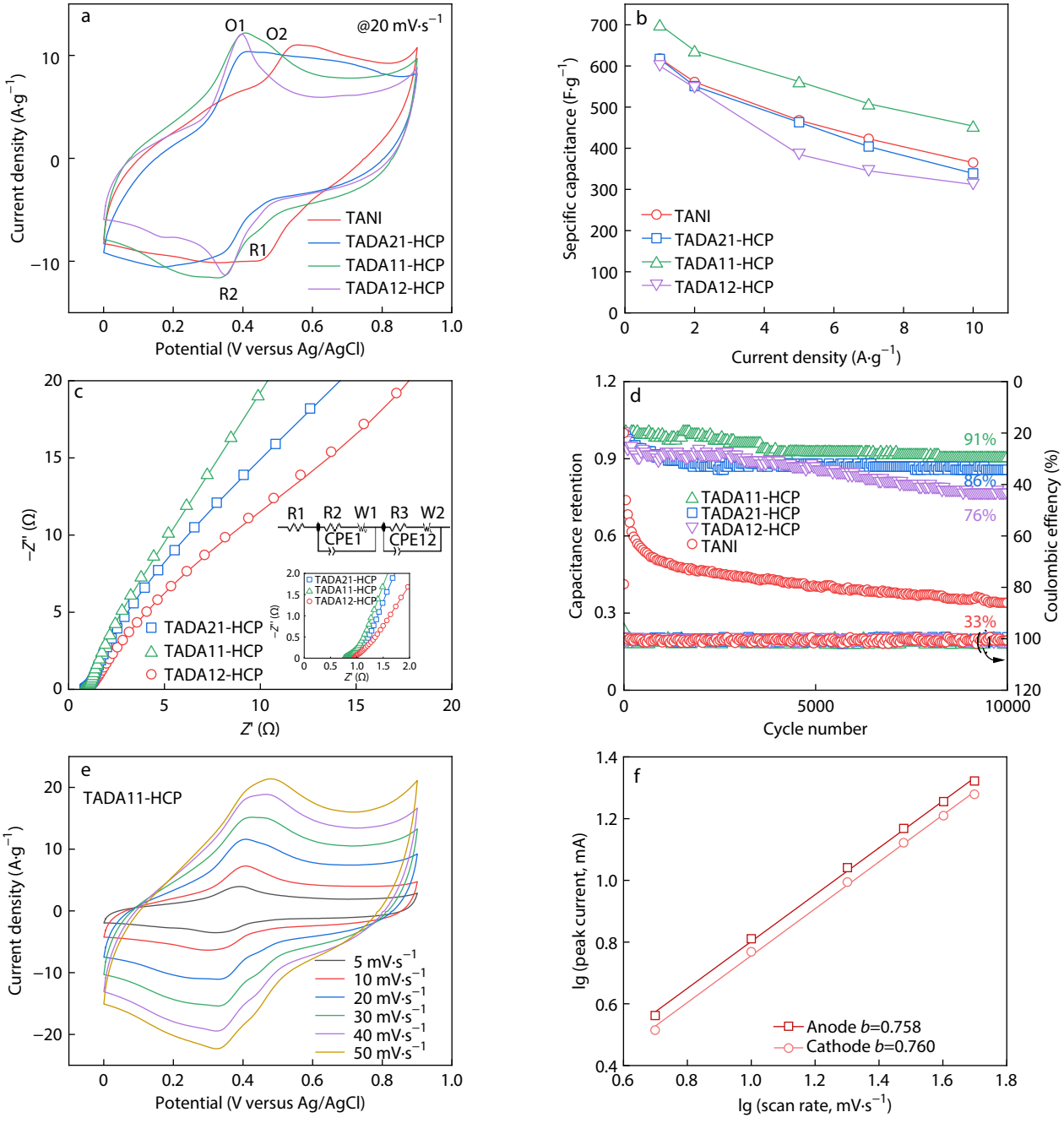

https://doi.org/10.1007/s10118-026-3623-8

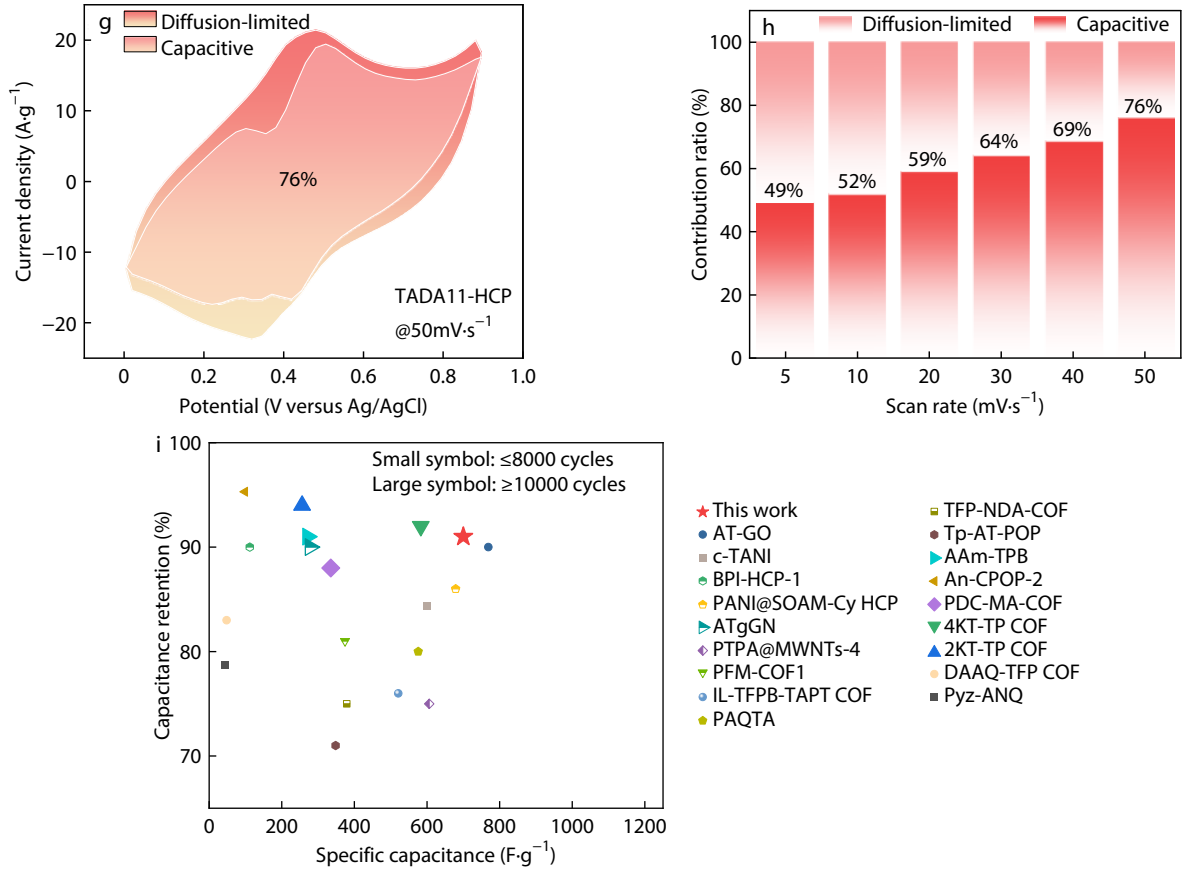

Fig. 2 (a) CV curves of TANI and TADA-HCPs at 50 mV·s^{-1}; (b) Evolution of the specific capacitance for TANI and TADA-HCPs measured across current densities of 1–10 A·g^{-1}; (c) Nyquist plots of the TADA-HCPs with fitting curves based on the R[C(RW)][C(RW)] equivalent circuit model; (d) Cycling stability and Coulombic efficiency of TANI and TADA-HCPs electrode over 10000 cycles at 2 A·g^{-1}; (e) CV curves of TADA11-HCP within scanning speeds of 5–50 mV·s^{-1}; (f) Correlation of log (peak current) with lg(scan rate) and corresponding best-fit line; (g) Separation analysis of capacitive and diffusion-controlled contributions to total charge storage of TADA11-HCP at 50 mV·s^{-1}; (h) Relative contributions of capacitive and diffusion-limited processes in TADA11-HCP at different scan rates, determined *via* Dunn's method; (i) Specific capacitance versus capacitance retention for TADA11-HCP and representative electrode materials reported in recent literature. Detailed electrochemical testing conditions, including electrolytes, current densities, and cycling numbers, are summarized in Table S1 (in ESI).

resistance (0.75 Ω) and better rate performance, confirming a favorable electronic structure for fast charge kinetics.[41] Cycling performance was assessed across 10000 cycles at 2 A·g^{-1} (Fig. 2d). TADA11-HCP exhibits outstanding durability, retaining 91% of its initial capacitance after the cycling test, which underscores the robustness of its hypercrosslinked network. In contrast, TANI retains only 33% of its capacitance after 10000 cycles, highlighting the superior cycling stability of TADA11-HCP compared to TANI. As shown in Fig. S9 (in ESI), the TANI electrode undergoes pronounced morphological collapse after long-term cycling, whereas the overall porous morphology of TADA11-HCP is well preserved (Fig. S10 in ESI). Moreover, the nearly unchanged FTIR spectra of TADA11-HCP before and after cycling (Fig. S11 in ESI) indicate excellent chemical stability of the redox-active framework during repeated charge-discharge processes, collectively accounting for its superior cycling durability.

To delve deeper into the storage process of charge in the TADA11-HCP electrode, we employed the Dunn method to quantitatively analyze its electrochemical kinetic behavior at different scan rates. By plotting log (peak currents) versus log (scan rate) for both anodic and cathodic processes (Fig. 2f), the calculated b values ranged between 0.5 and 1.0. This result indicates that charge storage in TADA11-HCP is a mixed-control process, simultaneously involving surface-controlled pseudocapacitive behavior (b=1) and diffusion-controlled Faradaic processes (b=0.5). To further quantify the contribution ratio of these two mechanisms, we analyzed and calculated the CV curves at different scan rates. As shown in Figs. 2(g) and 2(h), increasing the scanning speed from 5 mV·s^{-1} to 50 mV·s^{-1} significantly elevated the pseudocapacitive contribution from 49% to 76% of the total capacitance.[42] This trend clearly reveals TADA11-HCP's dual charge storage dynamics: at low scan rates, ions have adequate time for diffusion into the electrode material, resulting in relatively prominent diffusion-controlled Faradaic redox reactions. Conversely, at high scan rates, ions predominantly undergo rapid Faradaic reactions with the electrode surface or near-surface regions, making surface-controlled pseudocapacitive behavior dominant.[43] Consequently, the surface-controlled pseudocapacitive behavior ensures rapid charge-discharge capability and excellent rate performance, while the diffusion-controlled bulk redox processes contribute to the high specific

capacitance of the electrode.[44] The synergistic interaction of these two mechanisms is key to achieving its high performance. To objectively assess the electrochemical performance of TADA11-HCP's supercapacitor electrode capabilities, its specific capacitance and cycling stability were evaluated in comparison to those of recently reported materials. As shown in Fig. 2(i) and Table S1 (in ESI), TADA11-HCP demonstrates a competitive balance between a high specific capacitance and excellent cycling stability among the reported systems.[12–14,21–23,26,36,45–51]

To clarify how TADA11-HCP can undergo redox reactions that can be reversed and to understand its energy storage process throughout the charging and discharging cycles, we used *ex situ* FTIR to track the changes in its structure in response to various applied voltages.[37,52] The representative charge-discharge profile at 0.1 A·g^{-1} is shown in Fig. 3(a). As shown in Fig. 3(b) and Fig. S12 (in ESI), the intensity of the band at 1665 cm^{-1} attributed to C=O stretching vibrations gradually decreased during discharge and recovered during subsequent charging, indicating that the carbonyl group in the AQ unit participated in reversible electrochemical reactions. Further semi-quantitative analysis of characteristic absorption peaks from the quinone and benzene rings revealed that the ratio of their integrated peak areas decreased from 1.44 to 0.90 during discharge and recovered to 1.29 after full discharge. This pattern indicates that part of the quinone structure was reduced to the benzene structure during discharge, with a reversible transformation occurring during charging. This behavior aligns with the typical quinone-benzene redox conversion mechanism observed in TANI.[53] Based on these results, it can be concluded that there is a possible charge storage mechanism, in which the −N= and C=O groups are the active sites. This mechanism not only preserves the inherent redox properties of TANI but also introduces additional Faradaic active sites through the incorporation of C=O functional groups, thereby significantly enhancing the pseudocapacitive performance of the material. Moreover, the hierarchical pore architecture of TADA11-HCP further amplified the utilization efficiency of these redox-active sites. The coexistence of micropores centered at approximately 1.6 nm and mesopores spanning 2–20 nm not only maximizes the exposure of electrochemically active −N= and C=O groups, but also facilitates rapid electrolyte infiltration and ion transport throughout the three-dimensional framework. In this configuration, micropores provide abundant accessible redox sites for Faradaic charge storage, while mesopores act as ion-buffering reservoirs and diffusion pathways, effectively alleviating mass-transport limitations during fast charge-discharge processes.

On this basis, the high capacitance of TADA-HCPs can be rationalized as follows. From a kinetic perspective, the high capacitance of TADA11-HCP was primarily governed by pseudocapacitive charge storage rather than diffusion-limited electric double-layer processes. As evidenced by the kinetic analysis derived from CV measurements (Figs. 2f–2h), the charge storage exhibited predominantly surface-controlled behavior, indicating that rapid Faradaic reactions occurring at or near the electrode surface play a dominant role.[43] In such systems, the overall capacitance is mainly dictated by the kinetics of redox reactions and the accessibility of electrochemically active sites, instead of the total surface area measured under N_2 adsorption conditions.[44,54] From a mechanistic viewpoint, the pseudocapacitive response originates from the reversible redox reactions of molecularly integrated −N= and C=O groups, as confirmed by the *ex situ* FTIR analysis. The reversible intensity changes of the C=O stretching vibration and the quinone/benzene conversion during charge-discharge processes directly demonstrate that these redox-active moieties participate in fast and highly reversible Faradaic reactions. Importantly, these active sites are uniformly embedded within the polymer backbone, enabling short electron-transport pathways and a high utilization efficiency of the available redox centers, even without relying on extremely high specific surface area. Furthermore, the hierarchical micro-/mesoporous architecture of TADA11-HCP plays a crucial synergistic role in translating these molecular redox reactions into high practical capacitance. Micropores maximize the exposure of redox-active −N= and C=O groups, while mesopores and interparticle voids facilitate rapid electrolyte infiltration and ion transport, thereby minimizing mass-transport resistance and sustaining fast pseudocapacitive kinetics during high-rate charge-discharge processes.[55] Therefore, the high capacitance of the TADA-HCPs originates from the synergistic combination of pseudocapacitive-dominated fast surface redox kinetics, the efficient utilization of abundant redox-active sites, and a favorable hierarchical pore structure.

To assess the practical application potential of the TADA11-HCP electrode material, a symmetric supercapacitor (TADA11-HCP||TADA11-HCP) was assembled using TADA11-HCP for both electrodes, employing 1 mol·L^{-1} H_2SO_4 aqueous solution as the electrolyte. The CV curves of this SSC exhibit distinct redox peaks and partial rectangular features within the possible voltage spectrum of −0.9 V to 0.9 V and −1.8 V to 1.8 V, indicating that its charge storage mechanism involves contributions from both Faraday pseudocapacitance and double-layer capacitance (Fig. S9a in ESI). When the operating voltage extends beyond 1.5 V, slight oxygen evolution due to water splitting can be observed. Fig. S9(b) (in ESI) shows the device's GCD profiles measured at 1 A·g^{-1}. The GCD curve exhibits distinct charge-discharge plateaus, further corroborating its pseudocapacitive behavior. As the voltage window broadeneds, the IR drop became progressively more pronounced. When operating at 1.2 V, the GCD curve exhibited an approximately symmetrical triangular shape, indicating highly reversible electrochemical reaction characteristics. Based on these results, we selected the optimized operating window of −1.2 V to 1.2 V for further investigation of the device's electrochemical performance. As shown in Fig. S10(a) (in ESI), increasing the sweep speed between 10–50 mV·s^{-1} maintained excellent shape stability in the CV profiles, with redox peaks and double-layer features remaining clearly distinguishable. GCD curves exhibited symmetrical shapes across different current densities without noticeable voltage drops (Fig. S10b in ESI), indicating low internal resistance and favorable rate performance.

To expand the application scope of the device and enhance its safety, we further assembled a quasi-solid-state

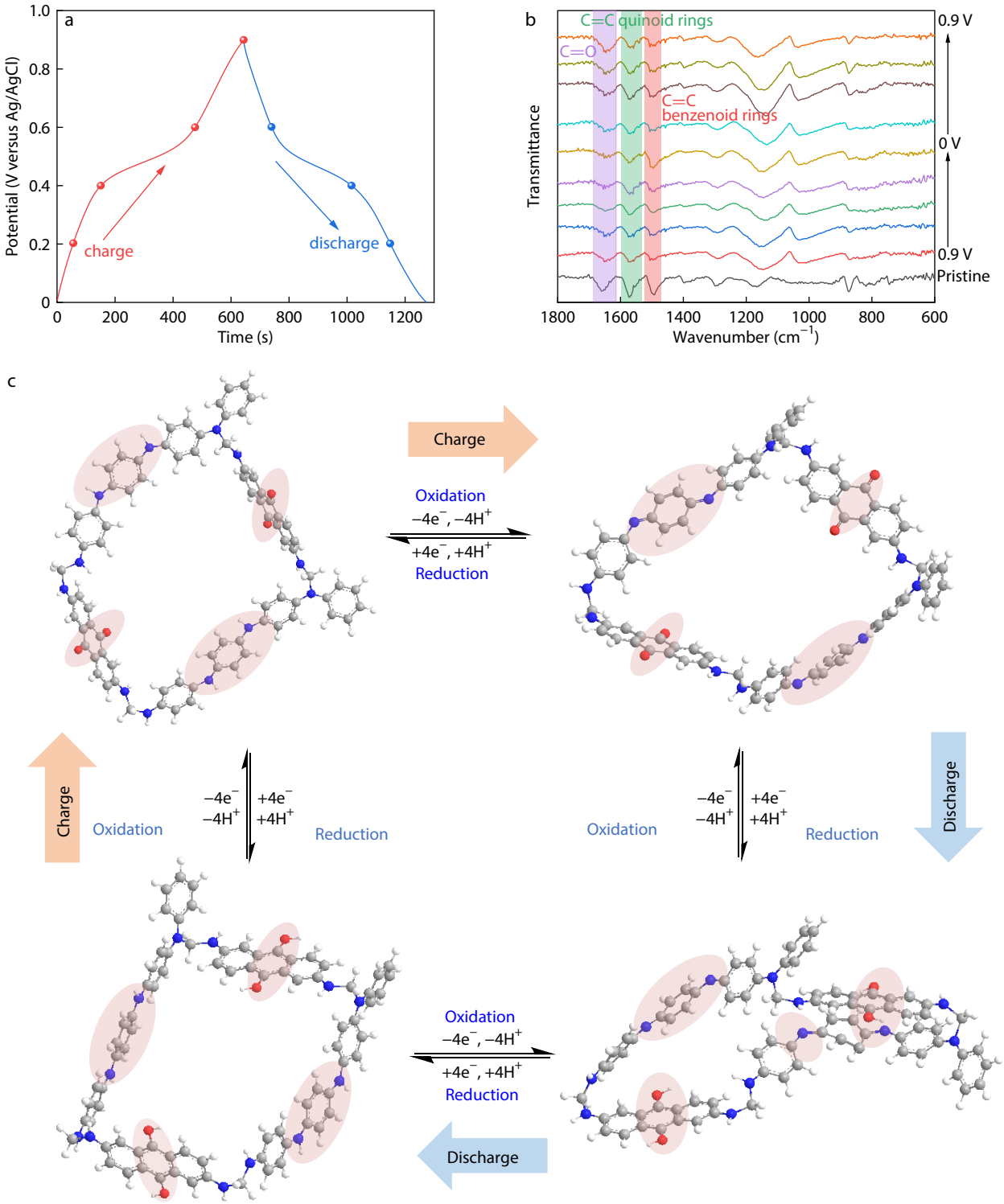

Fig. 3 Proposed charge/discharge mechanism. (a) Discharge/charge curve of TADA11-HCP (0.1 A·g^{-1}); (b) *Ex situ* FTIR analysis of TADA11-HCP; (c) Charge/discharge mechanism of TADA-HCPs.

symmetric supercapacitor (TADA11-HCP||TADA11-HCP) using a PVA/H_2SO_4 gel electrolyte. Figs. 4(a) and 4(b) present the CV and GCD profiles of the device across various voltage windows. As observed in Fig. 4(a), the CV curves display typical pseudocapacitive behavior, featuring distinct redox peaks. A noticeable oxygen evolution reaction peak appeared when the potential reaches 1.2 V, indicating the onset of oxygen evolution at this voltage. Such behavior has been commonly reported in PVA-based gel electrolytes and is generally associated with polymer–electrolyte interactions that regulate the

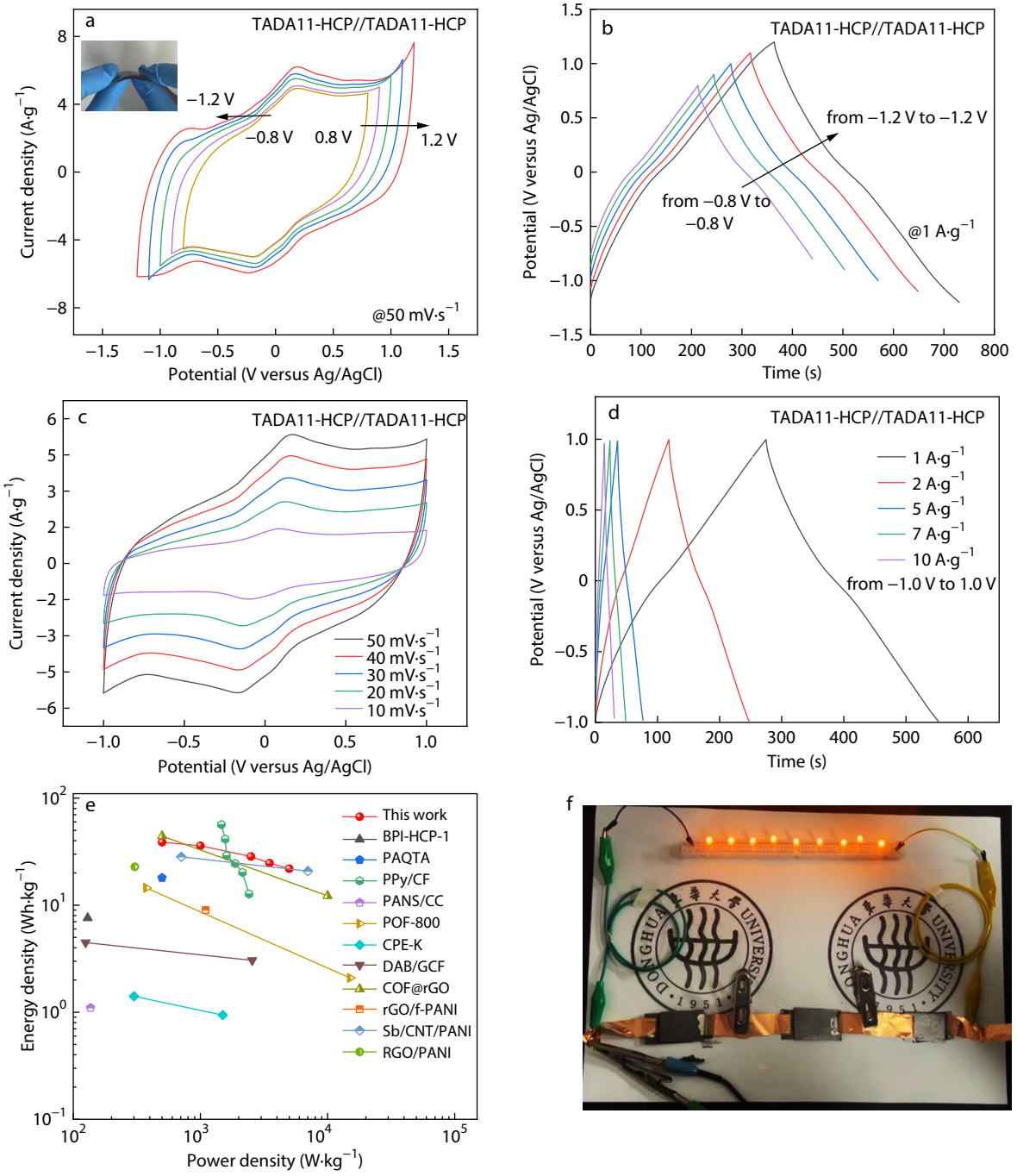

Fig. 4 (a) CV curves of the TADA11-HCP-based quasi-solid-state SSC measured at different voltage windows; (b) GCD profiles of the TADA11-HCP-based quasi-solid-state SSC recorded at different voltage windows; (c) CV curves of the TADA11-HCP-based quasi-solid-state SSC at various scan rates within a voltage window from −1.2 V to 1.2 V; (d) GCD profiles of the TADA11-HCP-based quasi-solid-state SSC at different current densities within a voltage window from −1.2 V to 1.2 V; (e) Ragone plot comparison of the TADA11-HCP-based quasi-solid-state SSC; (f) Optical image of multiple LEDs simultaneously powered by three series-connected quasi-solid-state supercapacitor devices.

kinetics and apparent onset of water-related side reactions.[56,57] Fig. 4(b) shows the GCD curves, which display almost symmetric triangular shapes, suggesting rapid charge/discharge responses and low internal resistance. Considering the oxygen evolution at higher potentials, a voltage window from −1.0 V to 1.0 V was selected for further investigation to avoid oxygen evolution and explore the electrochemical behavior of the quasi-solid-state SSC. Figs. 4(c) and 4(d) present the CV curves from 10 mV·s^{-1} to 50 mV·s^{-1} and the GCD profiles between 1 and 10 A·g^{-1}, respectively. As illustrated in Fig. 4(c), the CV profiles maintained a quasi-symmetric shape across the entire sweep speed range from 10 mV·s^{-1} to 50 mV·s^{-1}, suggesting fast electrode kinetics and excellent electrochemical reversibility. Based on the GCD data

shown in Fig. 4(d), the quasi-solid-state symmetric supercapacitor exhibits 278.4 $F \cdot g^{-1}$ specific capacitance when measured at 1 $A \cdot g^{-1}$ and it still maintains a 57% capacitance rating even when subjected to a substantial current density of 10 $A \cdot g^{-1}$ (Fig. S11 in ESI), demonstrating exceptional rate capability and good power output performance. To further evaluate the energy storage characteristics of the quasi-solid-state device, we calculated its energy and power densities from the GCD data. The device achieves a 38.7 $Wh \cdot kg^{-1}$ energy density and a power density of 500.43 $W \cdot kg^{-1}$ at 1 $A \cdot g^{-1}$. When cranking up the current density to 10 $A \cdot g^{-1}$, the power density significantly rises to 4996.20 $W \cdot kg^{-1}$, while the energy density remains at 21.9 $Wh \cdot kg^{-1}$ (Table S2 in ESI). This energy-power relationship indicates that the quasi-solid-state supercapacitor is capable of maintaining effective energy output over a wide power range, demonstrating excellent overall energy storage performance. To objectively evaluate the overall energy-storage performance, a Ragone plot was constructed for the TADA11-HCP-based quasi-solid-state SSC and compared with the recently reported SSC. As shown in Fig. 4(e),[22,26,58–66] the data points of the present device fall within the region characteristic of high-performance supercapacitors, exhibiting competitive values in both energy density and power density. This comparison further confirms the remarkable capability of the device to balance high-energy output with high-power delivery. As shown in Fig. 3(f) and Video S1 (in ESI), by connecting multiple devices in series, we successfully illuminated a row of yellow LEDs, providing intuitive evidence for the practical potential of TADA11-HCP-based supercapacitors in flexible electronic devices.

CONCLUSIONS

In this study, a series of hyper-crosslinked polymers (TADA-HCPs) based on TANI and DAQ were successfully designed and synthesized. Through molecular structure regulation and hypercrosslinking reactions, a pseudocapacitive electrode material was constructed that combines high specific capacitance with excellent cycling stability. Systematic characterization confirmed that TADA-HCPs successfully integrated TANI's redox activity, additional quinone active sites provided by DAQ, and high porosity derived from hypercrosslinked structures, achieving synergistic optimization of structure and function at the molecular level. Electrochemical performance tests indicated that the TADA11-HCP material exhibited optimal comprehensive properties, with an impressive specific capacitance of 700 $F \cdot g^{-1}$ at 1 $A \cdot g^{-1}$, coupled with capacitance retention rate as high as 91% after 1×10^4 cycles at 2 $A \cdot g^{-1}$. Conversely, the pristine TANI electrode maintains only 33% of its original capacitance under the same cycling conditions. This good performance stems from its balanced electronic structure, well-developed micro-/mesoporous composite porouse network, and low charge transfer resistance. Kinetic analysis indicated that the excellent electrochemical performance of TADA11-HCP originates from the synergistic contribution of electric double-layer capacitance and fast pseudocapacitive Faradaic reactions enabled by its hierarchical porous architecture and redox-active functional groups. Furthermore, a quasi-solid-state SSC was fabricated using the TADA11-HCP electrodes and PVA/H_2SO_4 gel electrolyte. The quasi-solid-state SSC delivers 278.4 $F \cdot g^{-1}$ at 1 $A \cdot g^{-1}$ and retained approximately 57% of its initial capacity at a high current density of 10 $A \cdot g^{-1}$. It achieved an energy density of 38.7 $Wh \cdot kg^{-1}$ at a power density of 500.43 $W \cdot kg^{-1}$, demonstrating good rate capability and effective energy output across a wide power range. In addition, several LEDs have been successfully powered by multiple devices connected in series, clearly demonstrating their practical potential in flexible electronic systems. This work gives insights into the design of porous materials for high performance, long-life supercapacitor electrode materials.

Conflict of Interests

The authors declare no interest conflict.

Electronic Supplementary Information

Electronic supplementary information (ESI) is available free of charge in the online version of this article at http://doi.org/10.1007/s10118-026-3623-8.

Data Availability Statement

The data that support the findings of this study are available on request from the corresponding authors upon reasonable request.

ACKNOWLEDGMENTS

This work was financially supported by the National Natural Science Foundation of China (Nos. 2473055 and 52373172), Shanghai Science and Technology Plan Project (No. 25DX1400200), the Key Technology Research and Development Program of Shanghai (No. 25CL290080), the Program of Shanghai Academic Research Leader (No. 21XD1420200), the Chang Jiang Scholar Program (No. T2023082), the Natural Science Foundation of Shanghai (No. 23ZR1401100), and the State Key Laboratory for Modification of Chemical Fibers and Polymer Materials (Nos. KF2204, KF2306, and KF2316).

REFERENCES

1 Seenivasan, S.; Adhikari, S.; Sivagurunathan, A. T.; Kim, D. H. Supercapatteries: Unlocking the potential of battery-supercapacitor fusion. *Energy Environ. Sci.* **2025**, *18*, 1054–1095.
2 Shin, S. J.; Gittins, J. W.; Balhatchet, C. J.; Walsh, A.; Forse, A. C. Metal-organic framework supercapacitors: challenges and opportunities. *Adv. Funct. Mater.* **2023**, *34*, 2308497.
3 Bhaduri, A.; Kim, C. E.; Ha, T. J. Recent developments in materials design for advanced supercapacitors. *Energy Environ. Mater.* **2025**, *8*, e70070.
4 Banerjee, S.; Mordina, B.; Sinha, P.; Kar, K. K. Recent advancement of supercapacitors: a current era of supercapacitor devices through the development of electrical double layer, pseudo and their hybrid supercapacitor electrodes. *J. Energy Storage* **2025**, *108*, 115075.
5 Iqbal, R.; Badshah, A.; Ma, Y. J.; Zhi, L. J. An electrochemically stable 2D covalent organic framework for high-performance

Graphical Abstract

Hypercrosslinked Porous Organic Polymers from Tetraaniline and Anthraquinone for High-capacitance, Long-life Supercapacitors

Xiao-Qian Gong, Xin-Ze-Yu Zhang, Yi-Fei Zhou, Yi Shi, Yu-Meng Zhang, Jia-Wei Hu, Peng-Cheng Li, Wei Lyu, and Yao-Zu Liao

Donghua University

A redox-active hypercrosslinked polymer integrating tetraaniline and anthraquinone enables high-capacitance and long-life supercapacitors by constructing a hierarchical porous architecture with high-density redox-active sites.

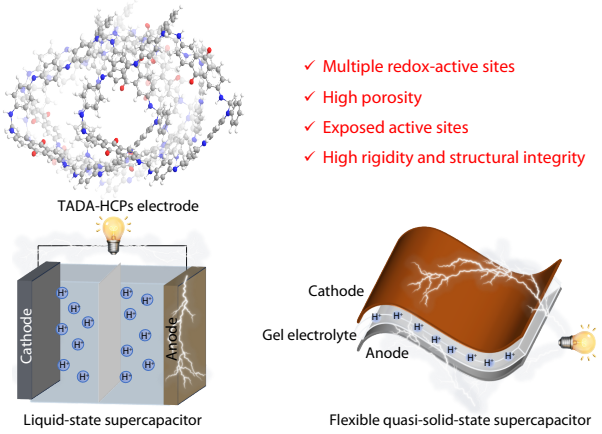

Chinese J. Polym. Sci. 2026, 44, 2212–2225 *https://doi.org/10.1007/s10118-026-3623-8*

organic supercapacitors. *Chinese J. Polym. Sci.* **2020**, *38*, 558–564.
6 Iqbal, R.; Ahmad, A.; Mao, L. J.; Ghazi, Z. A.; Imani, A.; Lu, C. X.; Xie, L. J.; Melhi, S.; Su, F. Y.; Chen, C. M.; Zhi, L.; Wei, Z. X. A high energy density self-supported and bendable organic electrode for redox supercapacitors with a wide voltage window. *Chinese J. Polym. Sci.* **2020**, *38*, 522–530.
7 Eftekhari, A.; Li, L.; Yang, Y. Polyaniline supercapacitors. *J. Power Sources* **2017**, *347*, 86–107.
8 Yan, S.; Guo, Z. F.; Ge, Z. Q.; Zhang, B. Y.; Zhang, Y. R.; Li, Y. S.; Wang, M. Z.; Ge, X. W. Study on the radiation synthesis mechanism and the electrochemical property of polyaniline. *Chinese J. Polym. Sci.* **2025**, *43*, 328–340.
9 Xie, M.; Kim, J. W.; Yang, Z.; Uemura, S.; Anderson, M.; Katsuyama, Y.; Kroes, B. C.; Chang, X.; Lin, C. W.; Kaner, R. B. Heterophase reduction of the fully oxidized aniline tetramer. *ACS Mater. Lett.* **2025**, *7*, 675–681.
10 Lin, C. W.; Chang, X.; Wang, Y.; Kaner, R. B. Conjugated aniline oligomers: more than just short pieces of conducting polyaniline. *Acc. Chem. Res.* **2025**, *58*, 3494–3505.
11 Wang, H.; Yu, Z.; El-Kady, M. F.; Anderson, M.; Kowal, M. D.; Li, M.; Kaner, R. B. Graphene/oligoaniline based supercapacitors: towards conducting polymer materials with high rate charge storage. *Energy Storage Mater.* **2019**, *19*, 137–147.
12 Yan, J.; Yang, L.; Cui, M.; Wang, X.; Chee, K. J.; Nguyen, V. C.; Kumar, V.; Sumboja, A.; Wang, M.; Lee, P. S. Aniline tetramer-graphene oxide composites for high performance supercapacitors. *Adv. Energy Mater.* **2014**, *4*, 1400781.
13 Tong, X.; Sheng, G.; Yang, D.; Li, S.; Lin, C. W.; Zhang, W.; Chen, Z.; Wei, C.; Yang, X.; Shen, F.; Shao, Y.; Wei, H.; Zhu, Y.; Sun, J.; Kaner, R. B.; Shao, Y. Crystalline tetra-aniline with chloride interactions towards a biocompatible supercapacitor. *Mater. Horiz.* **2022**, *9*, 383–392.
14 Chang, X.; El-Kady, M. F.; Huang, A.; Lin, C. W.; Aguilar, S.; Anderson, M.; Zhu, J. Z. J.; Kaner, R. B. 3D graphene network with covalently grafted aniline tetramer for ultralong-life supercapacitors. *Adv. Funct. Mater.* **2021**, *31*, 2102397.
15 Tan, L.; Tan, B. Hypercrosslinked porous polymer materials: design, synthesis, and applications. *Chem. Soc. Rev.* **2017**, *46*, 3322–3356.
16 Wood, C. D.; Tan, B.; Trewin, A.; Niu, H. J.; Bradshaw, D.; Rosseinsky, M. J.; Khimyak, Y. Z.; Campbell, N. L.; Kirk, R.; Stöckel, E.; Cooper, A. I. Hydrogen storage in microporous hypercrosslinked organic polymer networks. *Chem. Mater.* **2007**, *19*, 2034–2048.
17 Germain, J.; Fréchet, J. M. J.; Svec, F. Hypercrosslinked polyanilines with nanoporous structure and high surface area: potential adsorbents for hydrogen storage. *J. Mater. Chem.* **2007**, *17*, 4989–4997.
18 Mohamed, M. G.; El-Mahdy, A. F. M.; Kotp, M. G.; Kuo, S.W. Advances in porous organic polymers: syntheses, structures, and diverse applications. *Mater. Adv.* **2022**, *3*, 707–733.
19 Sun, H.; Li, J.; Liang, W.; Gong, X.; Jing, A.; Yang, W.; Liu, H.; Ren, S. Porous organic polymers as active electrode materials for energy storage applications. *Small Methods* **2024**, *8*, e2301335.
20 Vinodh, R.; Gopi, C. V. V. M.; Kummara, V. G. R.; Atchudan, R.; Ahamad, T.; Sambasivam, S.; Yi, M.; Obaidat, I. M.; Kim, H. J. A review on porous carbon electrode material derived from hypercross-linked polymers for supercapacitor applications. *J. Energy Storage* **2020**, *32*, 101831.
21 Mohamed, M. G.; Zhang, X.; Mansoure, T. H.; El-Mahdy, A. F. M.; Huang, C. F.; Danko, M.; Xin, Z.; Kuo, S. W. Hypercrosslinked porous organic polymers based on tetraphenylanthraquinone for CO_2 uptake and high-performance supercapacitor. *Polymer* **2020**, *205*, 122857.
22 Goudar, S. H.; Dash, R.; Babu, D. J.; Kurra, N.; Venkata Rao, K. Rational design strategy for the synthesis of hyper-cross-linked polymers using dipolar π-systems and proton sorption induced pseudocapacitance. *ACS Appl. Energy Mater.* **2025**, *8*, 4494–4500.
23 Kotp, M. G.; Kuo, S. W. Enhanced electrochemical performance of polyaniline and hyper-crosslinked porous polymer composite for advanced supercapacitor applications. *Electrochim. Acta* **2025**, *531*, 146440.

24 Bi, J.; Bao, K.; Zhao, M.; Zha, Y.; Chen, T.; Huang, C.; Lv, Z. Novel phenol-functionalized hypercrosslinked polymer for efficient tetracycline and iodine adsorption. *Appl. Surf. Sci.* **2025**, *688*, 162385.

25 Yin, Q.; Xiao, L.; Wei, Q.; Meng, C.; He, Y.; Song, S.; Zhou, Y.; Qiang, R.; Yang, Y.; Li, Z.; Hu, Z. 2,6-Diaminoanthraquinone covalently crosslinked graphene network noncovalently modified by indanthrone as an organic molecular electrode for supercapacitor. *J. Energy Storage* **2025,** *107*, 114841.

26 Liao, Y.; Wang, H.; Zhu, M.; Thomas, A. Efficient supercapacitor energy storage using conjugated microporous polymer networks synthesized from buchwald-hartwig coupling. *Adv. Mater.* **2018**, *30*, e1705710.

27 Liu, H.; Teng, L.; He, W.; Duan, J.; Gong, X.; Mi, X.; Zhuang, Y.; Sun, B.; Lyu, W.; Liao, Y. Synergistic modulation of band gap and porosity in conjugated microporous polymers for high-rate lithium-ion storage. *ACS Appl. Energy Mater.* **2025**, *8*, 9760–9769.

28 Vicha, J.; Novotný, J.; Komorovský, S.; Straka, M.; Kaupp, M.; Marek, R. Relativistic heavy-neighbor-atom effects on NMR shifts: concepts and trends across the periodic table. *Chem. Rev.* **2020**, *120*, 7065–7103.

29 Begni, F.; Gullo, F.; Paul, G.; Rea, R.; Ferrari, M. C.; Mangano, E.; Cossi, M.; Gatti, G.; Marchese, L. Optimization of the friedel-crafts alkylation for the synthesis of hyper-cross-linked polymers. *ACS Appl. Polym. Mater.* **2022**, *4*, 5281–5286.

30 Sharma, V.; Khilari, S.; Pradhan, D.; Mohanty, P. Solvothermally synthesized nanoporous hypercrosslinked polyaniline: Studies of the gas sorption and charge storage behavior. *RSC Adv.* **2016**, *6*, 56421–56428.

31 Zhao, Q.; Ni, Y.; Lu, Y.; Xie, W.; Li, H.; Yan, Z.; Zhang, K.; Li, Y.; Chen, J. Dual active site covalent organic framework anode enables stable aqueous proton batteries. *Angew. Chem. Int. Ed.* **2025**, *64*, e202424025.

32 Gokkus, K. New hyper-crosslinked polymers for enhanced CO_2 adsorption: synthesis and characterization. *Sustain. Chem. Pharm.* **2025**, *45*, 102015.

33 Kruk, M.; Jaroniec, M. Gas adsorption characterization of ordered organic-inorganic nanocomposite materials. *Chem. Mater.* **2001**, *13*, 3169–3183.

34 Bhadra, S.; Khastgir, D. Extrinsic and intrinsic structural change during heat treatment of polyaniline. *Polym. Degrad. Stabil.* **2008**, *93*, 1094–1099.

35 Señorans, S.; Valencia, I.; Merino, E.; Iglesias, M.; Fernández-Rodríguez, M. A.; Maya, E. M. Hyper-cross-linked porous polymer featuring B-N covalent bonds (HCP-BNs): a stable and efficient metal-free heterogeneous photocatalyst. *ACS Macro Lett.* **2023**, *12*, 949–954.

36 Li, M.; Liu, J.; Li, Y.; Xing, G.; Yu, X.; Peng, C.; Chen, L. Skeleton engineering of isostructural 2D covalent organic frameworks: orthoquinone redox-active sites enhanced energy storage. *CCS Chem.* **2021**, *3*, 696–706.

37 Zhang, X.; Teng, L.; Chen, J.; Gong, X.; Liu, H.; Duan, J.; Jiang, L.; Hou, X.; Lyu, W.; Liao, Y. Conjugated microporous polymers via a one-pot buchwald-hartwig/suzuki-miyaura double-coupling for high-performance flexible supercapacitors. *J. Colloid Interface Sci.* **2026**, *701*, 138671.

38 Lyu, W.; Yan, C.; Chen, Z.; Chen, J.; Zuo, H.; Teng, L.; Liu, H.; Wang, L.; Liao, Y. Spirobifluorene-based conjugated microporous polymer-grafted carbon nanotubes for efficient supercapacitive energy storage. *ACS Appl. Energy Mater.* **2022**, *5*, 3706–3714.

39 Yang, Y.; Ma, W.; Zhu, H.; Meng, H.; Wang, C.; Ma, F.; Hu, Z. Graphene covalently functionalized with 2,6-diaminoanthraquinone (DQ) as a high performance electrode material for supercapacitors. *New J. Chem.* **2020**, *44*, 16821–16830.

40 Yuan, W.; Weng, J.; Sun, Y.; Zhang, P.; Ding, M.; Chen, S.; Zhou, P.; Zhou, J. A novel hierarchical porous covalent organic framework as multi-active-center anode for high-performance sodium ion capacitors. *Adv. Funct. Mater.* **2024**, *35*, 2415402.

41 Li, H.; Cao, M.; Wang, R.; Xiong, P.; Liu, Y.; Zhang, L.; Zhang, L.; Zhang, L.; Chao, D.; Zhang, C. Design strategy for small-molecule organic cathodes: Regulated active groups enable high capacity and voltage in aqueous and seawater aluminum ion batteries. *Angew. Chem. Int. Ed.* **2025**, *64*, e202508057.

42 Ren, J.; Su, X.; Zhang, X.; Yan, X.; Wang, H. G.; Chen, L. A pyrazine-based two-dimensional conjugated metal-organic framework for air self-charging aqueous zinc-ion batteries. *CCS Chem*. **2026**, *8*, 341–349.

43 Wang, J.; Polleux, J.; Lim, J.; Dunn, B. Pseudocapacitive contributions to electrochemical energy storage in TiO_2 (anatase) nanoparticles. *J. Phys. Chem. C* **2007**, *111*, 14925–14931.

44 Augustyn, V.; Simon, P.; Dunn, B. Pseudocapacitive oxide materials for high-rate electrochemical energy storage. *Energy Environ. Sci.* **2014**, *7*, 1597–1614.

45 Zuo, H.; Duan, J.; Lyu, B.; Lyu, W.; Li, Y.; Mei, X.; Liao, Y. Carbon nanotube template-assisted synthesis of conjugated microporous polytriphenylamine with high porosity for efficient supercapacitive energy storage. *Macromol. Rapid Commun.* **2023**, *45*, 2300238.

46 Biradar, M. R.; Rao, C. R. K.; Bhosale, S. V.; Bhosale, S. V. Flame-retardant 3D covalent organic framework for high-performance symmetric supercapacitors. *Energy Fuels* **2023**, *37*, 4671–4681.

47 Liu, X.; Yang, F.; Wu, L.; Zhou, Q.; Ren, R.; Lv, Y. k. Ionic liquid-loaded covalent organic frameworks with favorable electrochemical properties as a potential electrode material. *Microporous Mesoporous Mater.* **2022**, *336*, 111906.

48 Hu, D.; Jia, Y.; Yang, S.; Huang, F.; Dong, Y.; Du, P. Redox-active 2D porous organic polymers for high-performance supercapacitor. *J. Ind. Eng. Chem.* **2023**, *123*, 320–329.

49 Yang, Z.; Liu, J.; Li, Y.; Zhang, G.; Xing, G.; Chen, L. Arylamine-linked 2D covalent organic frameworks for efficient pseudocapacitive energy storage. *Angew. Chem. Int. Ed.* **2021**, *60*, 20754–20759.

50 Li, L.; Lu, F.; Xue, R.; Ma, B.; Li, Q.; Wu, N.; Liu, H.; Yao, W.; Guo, H.; Yang, W. Ultrastable triazine-based covalent organic framework with an interlayer hydrogen bonding for supercapacitor applications. *ACS Appl. Mater. Interfaces* **2019**, *11*, 26355–26363.

51 Biradar, M. R.; Salkar, A. V.; Morajkar, P. P.; Bhosale, S. V.; Bhosale, S. V. Pyrazine-based organic electrode material for high-performance supercapacitor applications. *J. Energy Storage* **2022**, *48*, 103953.

52 Sun, T.; Li, Z. J.; Yang, X.; Wang, S.; Zhu, Y. H.; Zhang, X. B. Imine-rich poly(o-phenylenediamine) as high-capacity trifunctional organic electrode for alkali-ion batteries. *CCS Chem.* **2019**, *1*, 365–372.

53 Yin, C.; Pan, C.; Pan, Y.; Hu, J.; Fang, G. Proton self-doped polyaniline with high electrochemical activity for aqueous zinc-ion batteries. *Small Methods* **2023**, *7*, e2300574.

54 Simon, P.; Gogotsi, Y. Materials for electrochemical capacitors. *Nat. Mater.* **2008**, *7*, 845–854.

55 Gong, X.; Zhang, X.; Wang, D.; Jing, C.; Zhang, Y. X. Three-dimensional graphene aerogel materials for supercapacitors: Strategies and mechanisms. *Energy Environ. Mater.* **2025**, *8*, e70054.

56 Teng, L.; Duan, J.; Liu, H.; Zhang, X.; Li, J.; Li, Y.; Hong, J.; Lyu, W.; Liao, Y. A conjugated microporous polymer-graphene composite porous sandwich-like film for highly efficient flexible supercapacitors. *J. Mater. Chem. A* **2024**, *12*, 12423–12434.

57 Li, C.; Zhu, X.; Wang, D.; Yang, S.; Zhang, R.; Li, P.; Fan, J.; Li, H.; Zhi, C. Fine tuning water states in hydrogels for high voltage aqueous

batteries. *ACS Nano* **2024**, *18*, 3101−3114.
58 Arvas, M. B.; Yaylagül, S.; Uzbiçen, K.; Koçyiğit, N.; Yağci, Ö. Impact of boehmite and gibbsite on the supercapacitor performances of polypyrrole: γ-AlO(OH)/PPy/CF and γ-$Al(OH)_3$/PPy/CF flexible and wearable nanocomposites. *J. Alloys Compd.* **2025**, *1016*, 178879.
59 Tian, Y.; Yang, Y.; Wu, Y.; Zhou, Z.; Li, Y.; Wang, J.; Liu, S.; Wang, C. Electropolymerization of 5-amino-2-naphthalenesulfonic acid and their application as the electrode material for supercapacitors. *J. Energy Storage* **2023**, *72*, 108308.
60 Vinodh, R.; Muralee Gopi, C. V. V.; Yang, Z.; Deviprasath, C.; Atchudan, R.; Raman, V.; Yi, M.; Kim, H. J. Novel electrode material derived from porous polymeric organic framework of phloroglucinol and terephthaldehyde for symmetric supercapacitors. *J. Energy Storage* **2020**, *28*, 101283.
61 Ha, N. T.; Yip, B. R. P.; Kusherbayev, A.; Bui Thi Thu, T.; Pham, T. T.; Bazan, G. C.; Nguyen, D. T. Exploring self-doped conjugated polyelectrolytes for all-polymer solid-state supercapacitors. *ACS Appl. Energy Mater*. **2025**, *8*, 18346−18354.
62 Dong, Y.; Wang, Y.; Zhang, X.; Lai, Q.; Yang, Y. Carbon-based elastic foams supported redox-active covalent organic frameworks for flexible supercapacitors. *Chem. Eng. J.* **2022**, *449*, 137858.
63 Yao, M.; Guo, C.; Geng, Q.; Zhang, Y.; Zhao, X.; Zhao, X.; Wang, Y. Construction of anthraquinone-containing covalent organic frameworks/graphene hybrid films for a flexible high-performance microsupercapacitor. *Ind. Eng. Chem. Res.* **2022**, *61*, 7480−7488.
64 Habib, H.; Wani, I. S.; Husain, S. High performance nanostructured symmetric reduced graphene oxide/polyaniline supercapacitor electrode: effect of polyaniline morphology. *J. Energy Storage* **2022**, *55*, 105732.
65 Jiang, Y.; Ou, J.; Luo, Z.; Chen, Y.; Wu, Z.; Wu, H.; Fu, X.; Luo, S.; Huang, Y. High capacitive antimonene/CNT/PANI free-standing electrodes for flexible supercapacitor engaged with self-healing function. *Small* **2022**, *18*, e2201377.
66 Zhao, Z.; Xu, A.; Zhang, S.; Cao, W.; Zhu, Y.; Yin, L.; Qin, Y. Scalable one-step synthesis of graphene/polyaniline films *via* dual-functional H_2SO_4 for supercapacitor electrodes. *Langmuir* **2025**, *41*, 24408−24417.

https://doi.org/10.1007/s10118-026-3623-8